iScience

CellPress
OPEN ACCESS

Article

Generic water-based spray-assisted growth for scalable high-efficiency carbon-electrode all-inorganic perovskite solar cells

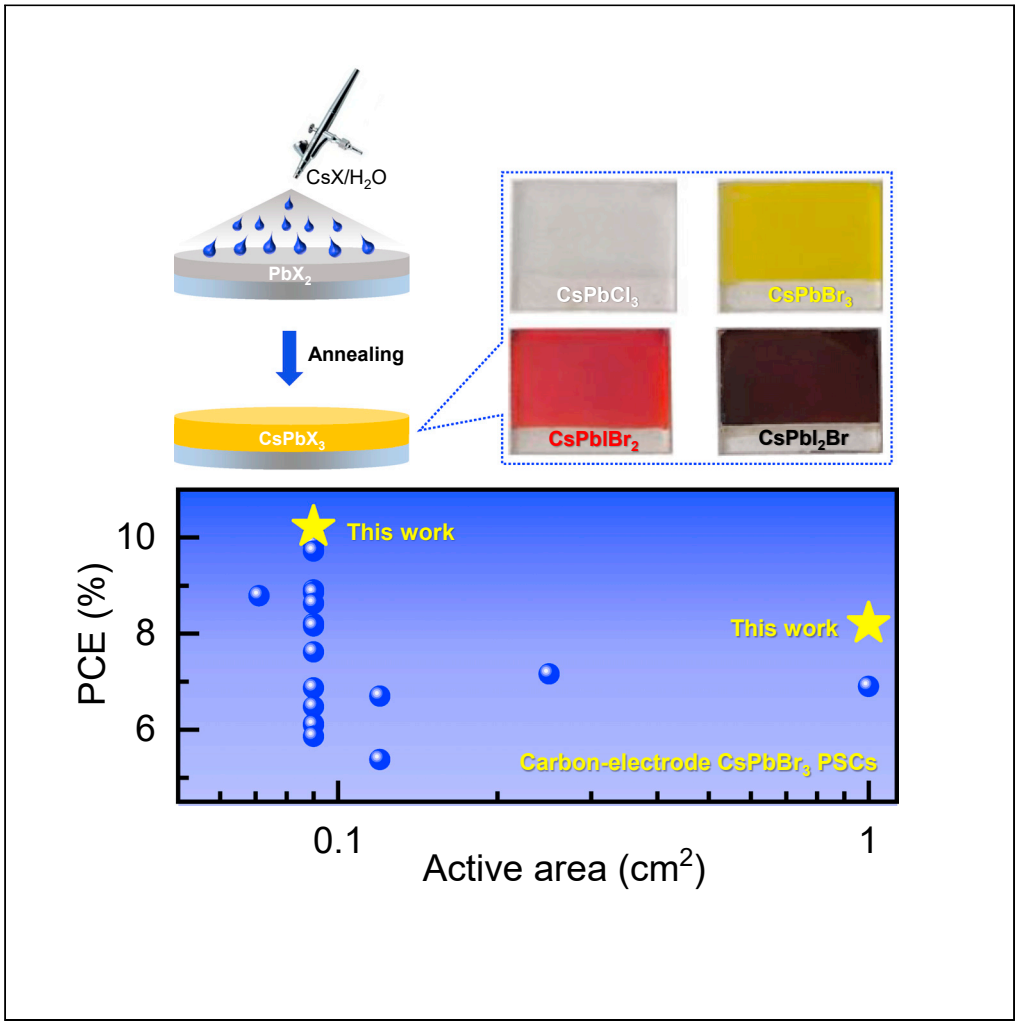

Zeyang Zhang, Yanshuang Ba, Dandan Chen, ..., Jincheng Zhang, Chunfu Zhang, Yue Hao

wdzhu@xidian.edu.cn (W.Z.)
cfzhang@xidian.edu.cn (C.Z.)

Highlights

Water-based spray-assisted growth is proposed for all-inorganic perovskite films

Water solvent makes perovskite films immune to microstructure of lead halide films

Record-high PCE of 10.22% is achieved for carbon-electrode $CsPbBr_3$ PSC

High PCEs are also attained for carbon-electrode $CsPbCl_3$, $CsPbIBr_2$, and $CsPbI_2Br$ PSCs

Zhang et al., iScience 24, 103365
November 19, 2021
https://doi.org/10.1016/j.isci.2021.103365

iScience

CellPress
OPEN ACCESS

Article

Generic water-based spray-assisted growth for scalable high-efficiency carbon-electrode all-inorganic perovskite solar cells

Zeyang Zhang,[1] Yanshuang Ba,[1] Dandan Chen,[2] Junxiao Ma,[1] Weidong Zhu,[1,*] He Xi,[1] Dazheng Chen,[1] Jincheng Zhang,[1] Chunfu Zhang,[1,3,*] and Yue Hao[1]

SUMMARY

A water-based spray-assisted growth strategy is proposed to prepare large-area all-inorganic perovskite films for perovskite solar cells (PSCs), which involves in spraying of cesium halide water solution onto spin-coating-deposited lead halide films, followed by thermal annealing. With $CsPbBr_3$ as an example, we show that as-proposed growth strategy can enable the films with uniform surface, full coverage, pure phase, large grains, and high crystallinity, which primarily benefits from the controllable CsBr loading quantity, and the use of water as CsBr solvent makes the reaction between CsBr and $PbBr_2$ immune to $PbBr_2$ film microstructure. As a result, the small-area (0.09 cm^2) and large-area (1.00 cm^2) carbon-electrode $CsPbBr_3$ PSCs yield the record-high efficiencies of 10.22% and 8.21%, respectively, coupled with excellent operational stability. We also illustrate that the water-based spray-assisted deposition strategy is suitable to prepare $CsPbCl_3$, $CsPbIBr_2$, and $CsPbI_2Br$ films with outstanding efficiencies of 1.27%, 10.44%, and 13.30%, respectively, for carbon-electrode PSCs.

INTRODUCTION

Perovskite solar cells (PSCs) have emerged as a promising candidate for photovoltaic power systems as per their high efficiency, low-cost raw materials, and straightforward fabrication process (Kojima et al., 2009; Park and Zhu, 2020; Rong et al., 2018). Their certified power conversion efficiency (PCE) of more than 25%, together with their enormously improved operational reliability, makes them particularly attractive (Li et al., 2021; Liu et al., 2021). However, the state-of-the-art PSCs are fabricated with organic-inorganic hybrid perovskite materials that contain volatile organic cations such as methylammonium (MA^+) or formamidinium (FA^+), which inherently result in the poor thermostability and photostability of resulting PSCs (Cheng and Ding, 2021; Chi and Banerjee, 2021; Li et al., 2020). Accordingly, researchers have shifted their attention toward all-inorganic perovskite alternatives (e.g., $CsPbX_3$, X = I, Br, Cl, or their mixtures) that are more robust against thermal and light stresses (Faheem et al., 2019; Ho-Baillie et al., 2019; Tian et al., 2020). In this way, carbon-electrode, all-inorganic PSCs have been proposed based on all-inorganic perovskite materials, which are free of organic, mutable hole-transporting layers and noble metal electrodes, thus possessing significant advantages in terms of production cost and stability (Duan et al., 2018b; Liang et al., 2016; Tian et al., 2020).

All-inorganic perovskite materials investigated for carbon-electrode, all-inorganic PSCs mainly include $CsPbI_3$ (Wang et al., 2021; Xiang et al., 2018, 2019), $CsPbI_2Br$ (Dong et al., 2019; He et al., 2020; Lin et al., 2020; Zhu et al., 2021), $CsPbIBr_2$ (Du et al., 2021; Zhu et al., 2018), and $CsPbBr_3$ (Chang et al., 2016; Duan et al., 2018b), and the performance of resulting carbon-electrode, all-inorganic PSCs has advanced rapidly in recent years. To be specific, since the first report of carbon-electrode $CsPbBr_3$ PSC in 2016 (Chang et al., 2016), its PCE has been promoted from 5.0% to 10.85% (Chang et al., 2016; Duan et al., 2020). When a hole booster composed of graphene oxide and $(NiCo)_{1-y}Fe_yO_x$ is adopted, the PCE of carbon-electrode $CsPbIBr_2$ PSC can reach up to 10.95% (Du et al., 2021). We demonstrated a top-seeded growth strategy in our laboratory which enables carbon-electrode $CsPbI_2Br$ PSC with a record-high PCE of 14.84% (Zhu et al., 2021). By use of a PbI_2-passivated $CsPbI_3$ film, a PCE of 14.6% was achieved for the PSC (Wang et al., 2021). Superior operational stability has also been demonstrated in carbon-electrode,

[1]State Key Discipline Laboratory of Wide Band Gap Semiconductor Technology & Shaanxi Joint Key Laboratory of Graphene, School of Microelectronics, Xidian University, Xi'an, Shaanxi 710071, PR China

[2]College of Science, Xi'an Shiyou University, Xi'an, Shaanxi 710065, PR China

[3]Lead contact

*Correspondence: wdzhu@xidian.edu.cn (W.Z.), cfzhang@xidian.edu.cn (C.Z.)

https://doi.org/10.1016/j.isci.2021.103365

all-inorganic PSCs. For example, Qi et al. (Tong et al., 2019a) reported a carbon-electrode $CsPbBr_3$ PSC that can retain 80% of its initial efficiency in ambient air for more than 2000 h without any encapsulation. When the surface of $CsPbI_2Br$ film is modified by hexyltrimethylammonium bromide (HTAB), the resulting PSC maintains 94% of the initial PCE after 2350-h storage and up to 90% of the initial PCE after aging for 330 h in a high-temperature (85°C) and medium-humidity (40%–60%) environment (Zhang et al., 2021). These significant achievements support the potential of carbon-electrode, all-inorganic PSCs for further development and practical applications.

Perovskite films with full coverage, enough thickness, pure phase, high crystallinity, and good uniformity are desired to fabricate large-area, high-efficiency PSCs for commercialization, either in a conventional or carbon-electrode configuration (Lee et al., 2020; Park and Zhu, 2020). The requirements for coverage, thickness, crystalline phase, and crystallinity guarantee high PCEs of resulting PSCs. Good uniformity is important to reduce the PCE gaps between the large-area PSCs and small-area ones, wherein it is generally necessary for large-scale (>800cm^2) PSCs to achieve similarly high PCEs with small-area PSCs for commercialization (Hu et al., 2019; Qiu et al., 2019). Some PCE loss is inevitable when the solar cell or module area increases, which is a more serious problem for PSCs than for other photovoltaic cells (Li et al., 2018). This disparity largely results from the fact that most of the PSCs are fabricated via spin coating method. This approach is not suitable for preparing the large-area, uniform perovskite films required for commercialization (Park and Zhu, 2020). This inapplicability is more prominent in inorganic perovskite films, as the solubilities of their precursor lead halide and cesium halide salt materials vary significantly in frequently used aprotic solvents such as dimethyl sulfoxide (DMSO) and N, N dimethylformamide (DMF) (Chen et al., 2020; Duan et al., 2018b; Sutton et al., 2016). Thus, the synthetic crystallization control of spin-coated films is not possible over large scales, and the non-uniformities in morphology and crystallinity become serious problems in large-area all-inorganic perovskite films (Chen et al., 2020). Meanwhile, spin coating must be conducted differently to produce inorganic perovskite films with different compositions, which makes the methodology for producing all-inorganic perovskite films extremely complex (Tian et al., 2020). Therefore, there is an urgent demand for a universal preparation strategy for large-area all-inorganic perovskite films with full coverage, high crystallinity, and good uniformity as the next step in securing effective, carbon-electrode, all-inorganic PSCs.

The spraying technique can be scaled up for large-area, uniform films, as is popular in the context of industrial manufacture (Krebs, 2009). This upscaling dramatically increases the utilization rate of precursor materials. Such a promising technique has been developed to prepare large-area, all-inorganic perovskite films (Li et al., 2018; Park and Zhu, 2020; Remeika and Qi, 2018; Swartwout et al., 2019). However, the record PCE of resulting all-inorganic PSCs with the conventional configuration is only 13.82% for 112-cm^2 devices based on composition-graded $CsPbI_2Br/CsPbI_{3-x}Br_x$ films (Heo et al., 2021). Moreover, the current spray deposition technology seems to require additional modification strategies to boost the performance of corresponding PSCs, as recently demonstrated by Liu et al. (Yu et al., 2021) On the other hand, the PCEs of carbon-electrode, all-inorganic PSCs fabricated by spraying are inferior. For example, spray-assisted deposition yielded a $CsPbBr_3$ PSC with an active area of 1 cm^2 and PCE of only 4.12% in a previous study (Duan et al., 2018a). The best-performing $CsPbIBr_2$ PSC prepared by spray-based method shows a stabilized PCE of only 6.3% (Lau et al., 2016). In addition, the spraying-based methods are still just practicable to all-inorganic perovskite films with specific compositions (Duan et al., 2018a; Yu et al., 2021; Zhou et al., 2018). Therefore, breakthroughs are needed for all-inorganic perovskite films to be manufactured by a scalable, universal spraying technique for carbon-electrode, all-inorganic PSCs, requiring understanding and control over the composition chemistry, fluid dynamics, and crystal growth behavior.

In this study, we developed a generic spray-assisted deposition strategy to produce all-inorganic perovskite films by innovatively adopting water as a benign solvent of cesium halide salts. Cesium halide solution is directly sprayed onto spin-coating-produced lead halide films under ambient conditions, followed by thermal annealing to promote the interdiffusion reaction between cesium halide and lead halide to form all-inorganic perovskite films. With $CsPbBr_3$ as an example, we demonstrate that full-coverage, pure-phase, large-grain films can be prepared by adjusting the loading dose of $CsBr/H_2O$ solution, which enables small-area (0.09 cm^2) carbon-electrode PSCs with optimized PCE of 10.22% and excellent operational stability. The use of water as the solvent of CsBr makes the reaction between CsBr and $PbBr_2$ immune to the underlying $PbBr_2$ film microstructure. Consequently, large-area, high-quality, uniform $CsPbBr_3$ films can be obtained with resulting carbon-electrode PSCs having an active area of 1 cm^2 and PCE of 8.21%. The PCEs

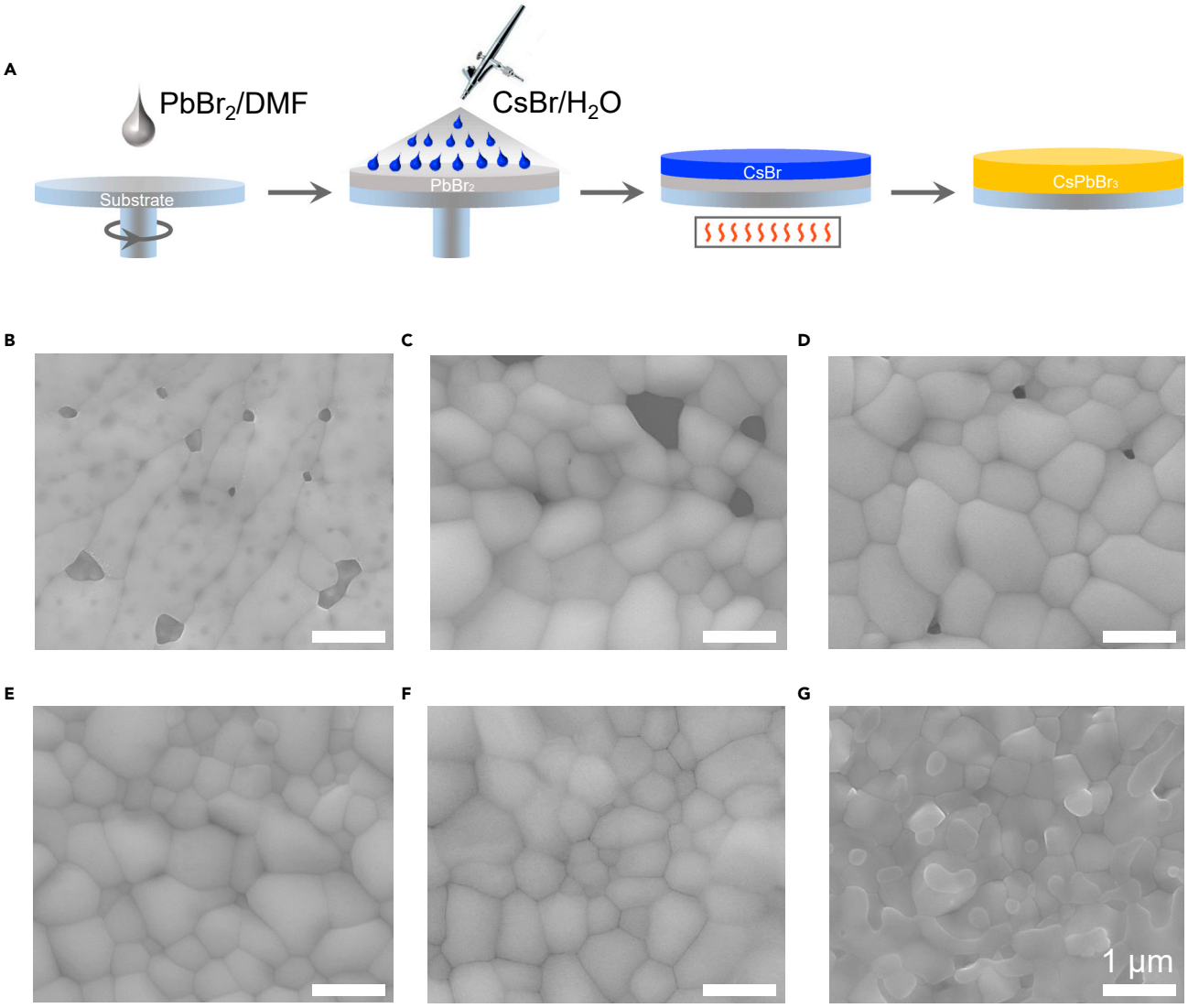

Figure 1. Illustration of water-based spray-assisted growth strategy and morphology characterizations of $PbBr_2$ film as well as $CsPbBr_3$ films

(A) Preparation of $CsPbBr_3$ film by water-based spray-assisted growth strategy.

(B–G) SEM images of (B) $PbBr_2$ and $CsPbBr_3$ films produced with (C) 30 μL, (D) 60 μL, (E) 90 μL, (F) 120 μL, and (G)150 μL $CsBr/H_2O$. All scale bars represent length of 1 μm.

we produced for both small- and large-area carbon-electrode $CsPbBr_3$ PSCs have the highest values among those with similar configurations reported previously. We explored the applicability of the water-based spray-assisted deposition strategy to prepare other all-inorganic perovskite films, wherein the well-crystalized, uniform $CsPbCl_3$, $CsPbIBr_2$, and $CsPbI_2Br$ films were obtained with similar recipes at PCEs of up to 1.27%, 10.44%, and 13.30% for resulting carbon-electrode PSCs, respectively. The results of this work may provide a feasible approach to scalable, high-efficiency carbon-electrode, all-inorganic PSCs.

RESULTS

Preparation of $CsPbBr_3$ films

Typical all-inorganic perovskite $CsPbBr_3$ was adopted as an example to illustrate the feasibility of water-based spray-assisted deposition in realizing high-quality, large-area, uniform all-inorganic perovskite films. The strategy is schematically depicted in Figure 1A. First, 100 μL of 1 M $PbBr_2$ solution was spin-coated onto TiO_2/FTO substrate to produce the $PbBr_2$ film. Next, 30, 60, 90, 120, or 150 μL of $CsBr/H_2O$ solution was

sprayed onto the surface of $PbBr_2$ film with a commercial airbrush connected to N_2 gas with 15-psi pressure. Finally, the sample was annealed at 250°C for 5 min to obtain a crystalline $CsPbBr_3$ film. Details of this process are given in the STAR Methods.

Morphology and structure of $CsPbBr_3$films

The morphologies of as-prepared $CsPbBr_3$ films were studied by scanning electron microscopy (SEM) as shown in Figures 1C–1G. For comparison, a SEM image of pristine $PbBr_2$ film is also provided in Figure 1B. The $PbBr_2$ film contains some randomly distributed pores, which support thorough contact of $PbBr_2$ with CsBr for complete transformation into $CsPbBr_3$ (Bing et al., 2020). As $CsPbBr_3$ formation is accompanied by the volume expansion of $PbBr_2$ film, these pores may release the micro-strain induced by volume expansion (Zhang et al., 2015). Pores and pinholes can still be observed in $CsPbBr_3$ films prepared with 30 and 60 μL of CsBr/H_2O, which indicates the incomplete conversion of $PbBr_2$ into $CsPbBr_3$. In other samples, the pores and/or pinholes disappear completely, resulting in $CsPbBr_3$ films composed of closely packed crystalline grains. The surfaces of $CsPbBr_3$ films formed with 90 and 120 μL of CsBr/H_2O are also relatively flat, while some surface bulges can be observed in the sample prepared with 150 μL of CsBr/H_2O. These bulge structures are presumed to be related to excess CsBr (Zhou et al., 2018). The average grain sizes are estimated to be 0.71, 0.80, 0.74, 0.69, and 0.64 μm for the $CsPbBr_3$ films prepared with 30, 60, 90, 120, and 150 μL CsBr/H_2O (Figure S1), respectively, all of which are comparable with those of previously reported $CsPbBr_3$ films (Chang et al., 2016; Duan et al., 2018b). Thus, $CsPbBr_3$ films with full coverage, flat surface, and large grains can be obtained via the proposed water-based spray-assisted deposition method after optimizing the volume of CsBr/H_2O.

Crystalline structures of the as-obtained $CsPbBr_3$ films were studied by X-ray diffraction (XRD). Figure 2A shows the XRD patterns and the magnified XRD results in the region of 2theta ranging from 10° to 14°. Diffraction peaks at 15.07°, 21.50°, 26.34°, and 30.61° can be detected in all the $CsPbBr_3$ films in accordance with previously reported perovskite $CsPbBr_3$ materials (Chang et al., 2016; Duan et al., 2018a; Duan et al., 2020; Tong et al., 2019a). By comparison, the sample prepared with 90 μL of CsBr/H_2O possesses the most intense (100) peak, indicating the highest crystallinity among the film samples. The $CsPb_2Br_5$ impurity phase can be identified in the $CsPbBr_3$ samples with 30 and 60 μL of CsBr/H_2O (Zhang et al., 2018), while the Cs_4PbBr_6 impurity phase can be observed in the films prepared with 120 and 150 μL of CsBr/H_2O (left panel, Figure 2A) (Zhang and Lin, 2020). However, both $CsPb_2Br_5$ and Cs_4PbBr_6 are absent from the $CsPbBr_3$ film prepared with 90 μL of CsBr/H_2O, which may be attributable to its relatively high crystallinity. The aforementioned XRD results make known that the pure-phase, high-crystallinity $CsPbBr_3$ film can be obtained by the proposed water-based spray-assisted growth strategy using 90 μL of CsBr/H_2O.

In $CsPbBr_3$ films, the formation of a $CsPb_2Br_5$ impurity phase is mainly caused by CsBr deficiency, while the Cs_4PbBr_6 impurity phase is largely related to excess CsBr, as shown in Figure 2B (Duan et al., 2018b; Zhang and Lin, 2020; Zhang et al., 2018). Cs_4PbBr_6 and/or $CsPb_2Br_5$ impurity phases are generally found in $CsPbBr_3$ films owing to the inherent difficulty of precise control over the CsBr dose (Duan et al., 2018b; Feng et al., 2020). These impurity phases generate undesirable energy barriers and trap states which hinder the transport and extraction of charge carriers and drive down PSC performance. $CsPbBr_3$ PSC performance is limited owing to this obstacle. In this study, we precisely controlled the loading amount of CsBr by adjusting the volume of CsBr/H_2O based on the water-based spray-assisted growth strategy. Our results show that this solution-processed $CsPbBr_3$ film is suitable for practical applications.

Optical properties of $CsPbBr_3$films

Figure 2C gives ultraviolet-visible (UV-vis) absorption spectra of the $CsPbBr_3$ films. A consistent absorption onset wavelength of ~523 nm and an exciton absorption peak at 509 nm can be observed for all films, which indicates that they have a similar bandgap of ~2.37 eV. The absorption values increase for the $CsPbBr_3$ films prepared with 30, 60, and 90 μL of CsBr/H_2O and then decrease for the samples obtained with 120 and 150 μL of CsBr/H_2O. The increased absorption intensities for the films produced with 30, 60, and 90 μL of CsBr/H_2O can be assigned to suppress or even eliminate $CsPb_2Br_5$ impurity phase, while the decreased absorption values for the samples prepared with 120 and 150 μL of CsBr/H_2O are largely related to the Cs_4PbBr_6 impurity phase they contain. $CsPb_2Br_5$ or Cs_4PbBr_6 impurity phases hold the bandgaps above 2.9 eV, so the films containing them have lower absorption intensities (Feng et al., 2020; Zhang and Lin, 2020; Zhang et al., 2018). Overall, the sample produced with 90 μL of CsBr/H_2O possesses the most intense absorption as it is composed of pure-phase $CsPbBr_3$, as the XRD results also suggest.

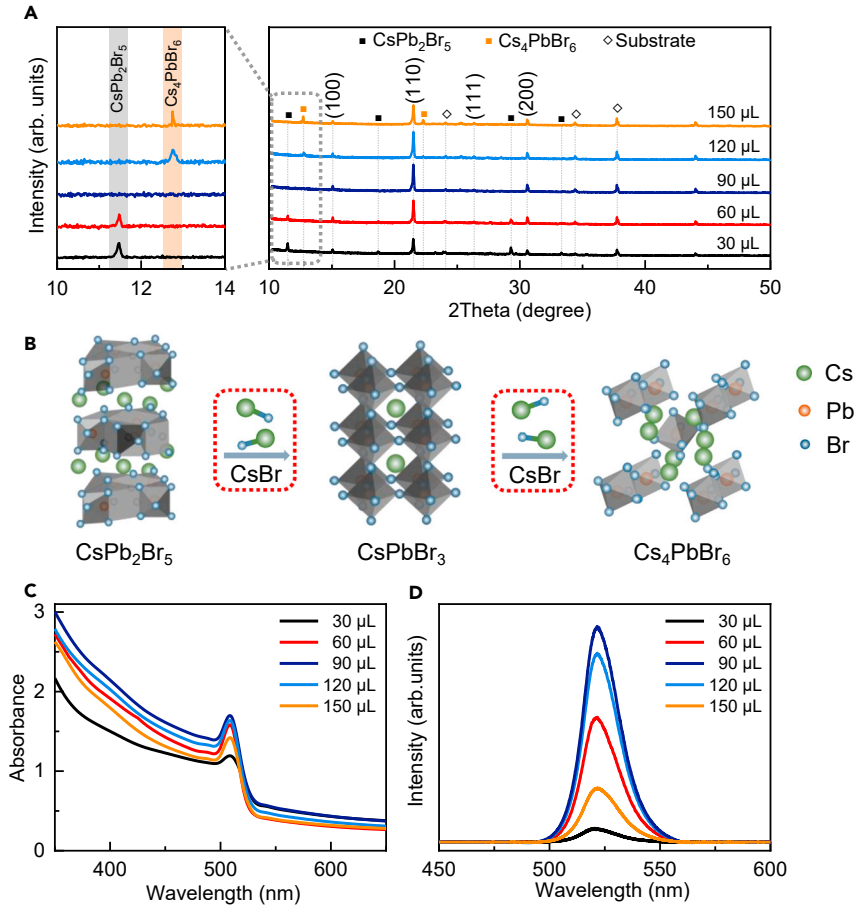

Figure 2. Crystal structure and optical characterizations of $CsPbBr_3$ films

(A) XRD patterns of $CsPbBr_3$ films produced with 30, 60, 90, 120, and 150 μL $CsBr/H_2O$. Left panel shows magnified XRD peaks from 10 to 14.

(B) Crystal structure models of $CsPb_2Br_5$, $CsPbBr_3$, and Cs_4PbBr_6; phase transition processes with increasing CsBr dose.

(C and D) (C) UV-vis absorption spectra and (D) steady-state PL spectra of $CsPbBr_3$ films.

Figure 2D shows the steady-state photoluminescence (PL) spectra of the $CsPbBr_3$ films grown on insulating substrates. A PL peak at ~522 nm can be detected in each of the films, which mainly originates from the band-to-band radiative recombination of photogenerated charge carriers. The PL peak intensifies in sequence for the $CsPbBr_3$ films prepared with 30, 60, and 90 μL of $CsBr/H_2O$ and then weakens gradually for those obtained with 120 and 150 μL of $CsBr/H_2O$. In this case, the sample produced with 90 μL of $CsBr/H_2O$ shows the highest PL peak intensity, which is indicative of the weakest non-radiative recombination of charge carriers it contains as well as its lack of impurity phase (Luo et al., 2020).

Solar cell performance

Carbon-electrode, all-inorganic PSCs were fabricated by following the layer stackings of $FTO/TiO_2/CsPbBr_3$/carbon to explore the photovoltaic performance of $CsPbBr_3$ films prepared with different doses of $CsBr/H_2O$. Figure 3A shows the SEM image of a representative PSC, where all the functional layers can be identified clearly. The thickness of $CsPbBr_3$ film is estimated to be ~340 nm, which is similar to that of previously reported $CsPbBr_3$ films prepared by two-step or multi-step methods (Chang et al., 2016; Duan et al., 2018b; Feng et al., 2020). Figure 3B gives the statistical PCEs of 20 individual carbon-electrode $CsPbBr_3$ PSCs fabricated with 30, 60, 90, 120, and 150 μL of $CsBr/H_2O$, the average PCEs of which are (4.37 ± 0.55)%, (6.96 ± 0.29)%, (9.34 ± 0.43)%, (7.71 ± 0.55)%, and (5.86 ± 0.36)%, respectively. The water-based spray-assisted growth strategy appears to be highly feasible to fabricate high-efficiency carbon-electrode $CsPbBr_3$ PSCs after the volume of $CsBr/H_2O$ solution is optimized.

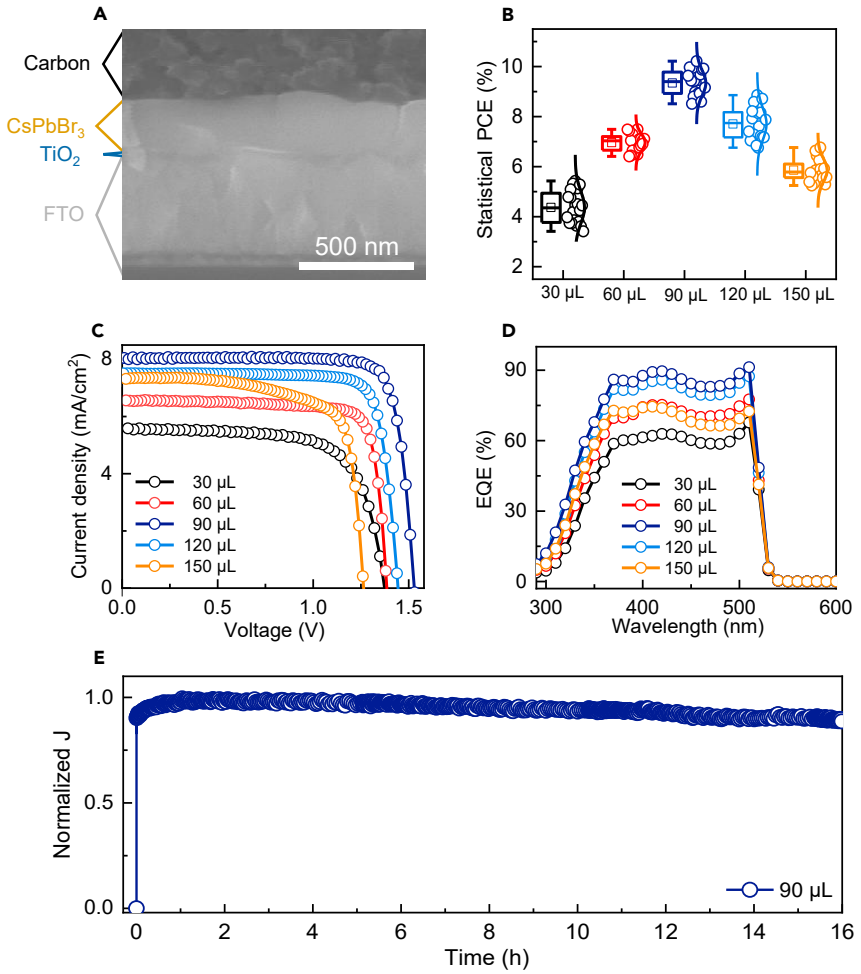

Figure 3. Photovoltaic performance and stability of carbon-electrode $CsPbBr_3$ PSCs

(A) Cross-sectional SEM image of a typical $CsPbBr_3$ PSC.

(B) Statistical PCEs of 20 individual PSCs based on $CsPbBr_3$ films produced with 30, 60, 90, 120, and 150 μL $CsBr/H_2O$. The scale bars in each of the statistical boxes represent the the maximum and minimum values, respectively.

(C and D) (C) J–V curves and (D) EQE spectra for best-performing $CsPbBr_3$ PSCs.

(E) Stabilized current density output near the maximum point of the champion $CsPbBr_3$ PSC obtained with 90 μL of $CsBr/H_2O$.

Figure 3C shows the current density versus voltage (J–V) curves of the best-performing carbon-electrode $CsPbBr_3$ PSCs fabricated with different volumes of $CsBr/H_2O$ solution, which were measured under simulated AM 1.5 G illumination and voltage scanning from 1.7 to −0.2 V. The resulting photovoltaic parameters, including J_{sc}, V_{oc}, FF, and PCE, are given in Table S1. The PCEs of related carbon-electrode $CsPbBr_3$ PSCs improve as $CsBr/H_2O$ dose increases from 30 to 90 μL. The value then decreases once the dose exceeds 90 μL. Variations in J_{sc}, V_{oc}, and FF follow the same trend with $CsBr/H_2O$ dose. Thus, the carbon-electrode $CsPbBr_3$ PSCs fabricated with 90 μL of $CsBr/H_2O$ have the best photovoltaic parameters among the PSCs. More importantly, its PCE of 10.22% stands the best value achieved for carbon-electrode $CsPbBr_3$ PSCs without any interface modification until now, as indicated by Table 1. The improved PCE of the carbon-electrode $CsPbBr_3$ PSC with increased $CsBr/H_2O$ dose from 30 to 90 μL can be attributed to a reduction in pores and/or pinholes as well as $CsPb_2Br_5$ impurity phase in the $CsPbBr_3$ film. The decreased PCE of $CsPbBr_3$ PSC is attributable to the Cs_4PbBr_6 impurity phase that emerges in the film when $CsBr/H_2O$ dose exceeds 90 μL.

External quantum efficiency (EQE) spectra of the carbon-electrode $CsPbBr_3$ PSCs are shown in Figure 3D, where an identical photocurrent onset wavelength of ~530 nm can be identified for all samples in

Table 1. Summary of PCE, V_{oc}, J_{sc}, and FF values of carbon-electrode $CsPbBr_3$ PSCs without any interface modification reported so far

Cell configuration	Area (cm^2)	V_{oc} (V)	J_{sc} (mA/cm^2)	FF	PCE (%)	Ref.
FTO/TiO_2/$CsPbBr_3$/carbon	0.09	1.528	8.06	0.83	10.22	This work
	1	1.397	7.84	0.75	8.21	
FTO/TiO_2/SnO_2/$CsPbBr_3$/carbon	0.071	1.310	8.24	0.814	8.79	Liu et al. (2019b)
	1	1.396	6.93	0.713	6.9	
FTO/c-TiO_2/$CsPbBr_3$/carbon	0.09	1.460	9.24	0.754	10.17	Tong et al. (2019b)
FTO/c-TiO_2/$CsPbBr_3$/carbon	0.09	1.413	9.55	0.73	9.86	Tong et al. (2019a)
FTO/c-TiO_2/$CsPbBr_3$/carbon	0.09	1.520	7.28	0.805	8.86	Zhang et al. (2019)
FTO/TiO_2/$CsPbBr_3$/carbon	0.09	1.370	7.66	0.82	8.63	Guo et al. (2019)
FTO/c-TiO_2/$CsPbBr_3$/carbon	0.09	1.430	7.32	0.78	8.16	Li et al. (2019)
FTO/TiO_2/$CsPbBr_3$/carbon	0.12	1.240	7.4	0.73	6.70	Liang et al. (2016)
FTO/c-TiO_2/$CsPbBr_3$/carbon	0.09	1.380	7.13	0.62	6.1	Liu et al. (2019a)
FTO/TiO_2/$CsPbBr_3$/carbon	0.09	1.340	6.46	0.68	5.86	Teng et al. (2018)
FTO/c-TiO_2/$CsPbBr_3$/carbon	0.12	1.130	6.79	0.70	5.38	Luo et al. (2018)

accordance with the absorption features of $CsPbBr_3$ films. The photocurrents appear to be generated by $CsPbBr_3$. EQEs in the whole response range are enhanced as $CsBr/H_2O$ dose increases from 30 to 90 μL and then begin to decline as the $CsBr/H_2O$ dose reaches 90 μL. The J_{sc} values integrated from the EQE spectra are 5.50, 6.43, 7.58, 7.25, and 6.27 mA/cm^2 for the carbon-electrode $CsPbBr_3$ PSCs prepared with 30, 60, 90, 120, and 150 μL $CsBr/H_2O$, respectively, which basically agrees with the light J-V curve results.

The working stability of the typical carbon-electrode $CsPbBr_3$ PSC prepared by 90 μL of $CsBr/H_2O$ was estimated under simulated AM 1.5G illumination and in ambient air with relative humidity (RH) of ~45% and temperature of ~25°C. Figure 3E shows the normalized photocurrent output near the maximum power point over 16 h. The photocurrent output is quite stable, and 90% of the initial value can be maintained after continuous testing, revealing the excellent operational stability of the carbon-electrode $CsPbBr_3$ PSC fabricated by the proposed strategy.

The proposed water-based spray-assisted growth strategy appears to enable full-coverage, pure-phase, large-grain $CsPbBr_3$ films with an optimized $CsBr/H_2O$ volume of 90 μL, ultimately yielding carbon-electrode PSCs with record-high efficiency and excellent operational stability. The uniformity of $PbBr_2$ film fabricated by the proposed method does not significantly influence the uniformity of the resulting $CsPbBr_3$ film. We used three $PbBr_2$ films with different uniformities to prepare respective $CsPbBr_3$ films to confirm this, noting the $PbBr_2$ films were prepared by adjusting the thermal treatment temperature to be 100°C, 150°C, and 200°C after the spin coating procedure. As shown in Figure 4A, $PbBr_2$ films with different surface appearances produced similar $CsPbBr_3$ films. In this case, a highly uniform $CsPbBr_3$ film of 10 × 10 cm^2 in size was prepared successfully as shown in Figure 4B. SEM images of the $PbBr_2$ films and the corresponding $CsPbBr_3$ films are shown in Figures 4C_1–4C_3 and 4D_1–4D_3. The microstructures of $PbBr_2$ films differ significantly in terms of surface coverage and grain morphology, but the resulting $CsPbBr_3$ films have comparable microstructures including uniform, flat, and closely packed crystalline grains with similar sizes. Thus, we conclude that the water-based spray-assisted growth strategy can effectively yield the large-area $CsPbBr_3$ films with satisfactory crystalline quality.

We noted that the desirable characteristics of the water-based spray-assisted growth strategy can be attributed to the reconstruction of $PbBr_2$ film induced by water solvent during spray-coating of $CsBr/H_2O$. To support our standpoint, the $PbBr_2$ films prepared with the thermal treatment temperature to be 100°C, 150°C, and 200°C were treated by directly spraying 90 uL of deionized water onto it, followed by annealing at 250°C for 5 min. The SEM images of the resulting $PbBr_2$ films are shown in Figures S2A–S2C. It is seen that the clear surface reconstruction of $PbBr_2$ film happens after the water treatment, which leads to the $PbBr_2$ films having the similar morphologic characters. Therefore, the final $CsPbBr_3$ films exhibit the alike surface appearances.

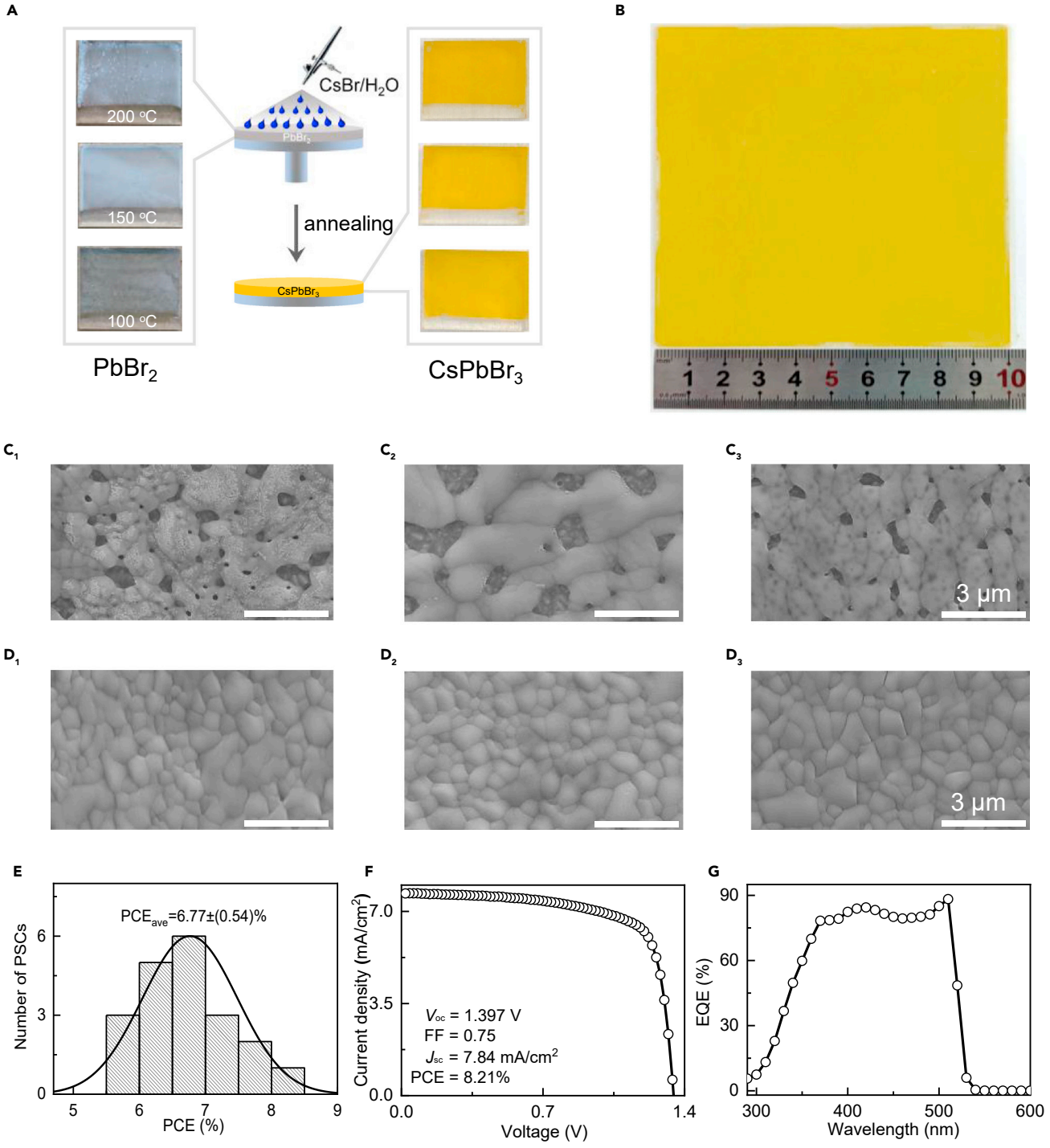

Figure 4. Photograph and morphology characterizations of $PbBr_2$ films and $CsPbBr_3$ films as well as photovoltaic performance of large-area carbon-electrode $CsPbBr_3$ PSCs

(A) Photographs of $PbBr_2$ films prepared with the different thermal treatment temperatures of 200°C, 150°C, and 100°C after the spin coating procedure, along with the $CsPbBr_3$ films prepared by water-based spray-assisted deposition.

(B) Photograph of $CsPbBr_3$ sample 10 × 10 cm^2 in size.

(C_1–C_3) SEM images of the $PbBr_2$ films with the thermal treatment temperature of (C_1) 200°C, (C_2) 150°C, and (C_3) 100°C.

(D_1–D_3) SEM images of $CsPbBr_3$ films produced with the $PbBr_2$ films with the thermal treatment temperature of (D_1) 200°C, (D_2) 150°C, and (D_3) 100°C.

(E) Statistical PCEs of 20 individual carbon-electrode $CsPbBr_3$ PSCs with active area of 1 cm^2.

(F and G) (F) J-V curve and (G) EQE spectrum for best-performing carbon-electrode $CsPbBr_3$ PSC with the active area of 1 cm^2.

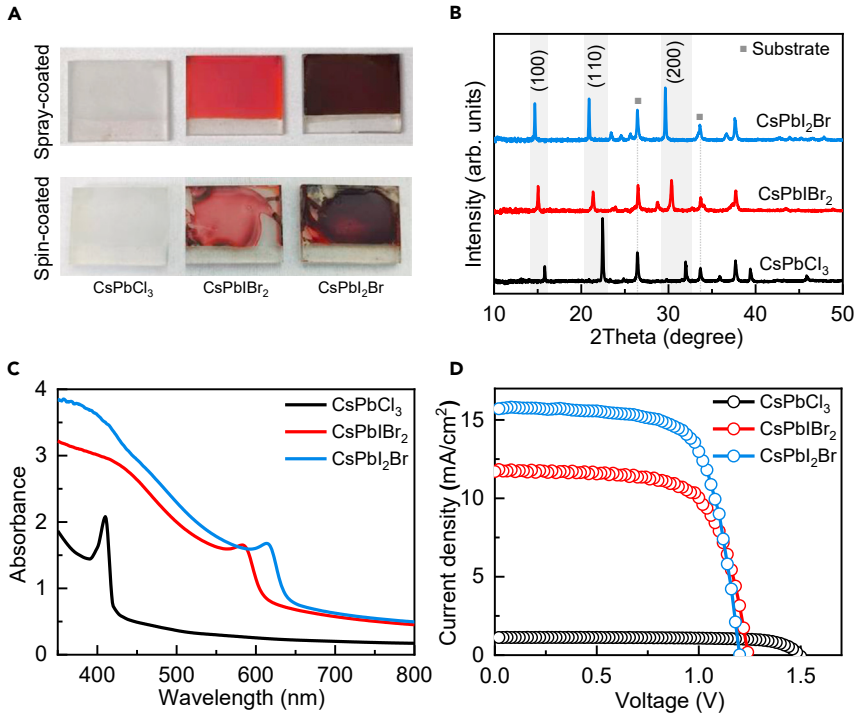

Figure 5. Visual, crystal structure, and optoelectronic characterization of all-inorganic perovskite films as well as photovoltaic performance of carbon-electrode, all-inorganic PSCs

(A) Photographs of $CsPbCl_3$, $CsPbIBr_2$, and $CsPbI_2Br$ films prepared by water-based spray-assisted deposition (top panel) and conventional two-step spin coating (bottom panel).

(B and C) (B) XRD patterns and (C) UV-vis absorption spectra of $CsPbCl_3$, $CsPbIBr_2$, and $CsPbI_2Br$ films prepared by water-based spray-assisted deposition.

(D) J-V curves for best-performing carbon-electrode, all-inorganic PSCs based on $CsPbCl_3$, $CsPbIBr_2$, and $CsPbI_2Br$ films.

Carbon-electrode $CsPbBr_3$ PSCs with a large active area of 1 cm^2 were also fabricated. Figure 4E shows the statistical PCEs of 20 PSCs obtained from five individual batches, wherein the average PCE is (6.77 $\pm$ 0.54)%. The J-V curve of the best-performing large-area carbon-electrode $CsPbBr_3$ PSC is shown in Figure 4F; its J_{sc}, V_{oc}, FF, and PCE are 7.84 mA/cm^2, 1.397 V, 0.75, and 8.21%, respectively. Notably, as also shown in Table 1, the PCE achieved here exceeds those of all previously reported large-area carbon-electrode $CsPbBr_3$ PSCs. The EQE spectrum shown in Figure 4G is similar to the small-area sample, and the integrated J_{sc} is in accordance with the J-V curve value, which validates the PCE test results from the J-V curves again.

We applied the proposed strategy to prepare other typical perovskite films for carbon-electrode, all-inorganic PSCs to explore its versatility. Similar to the optimized preparation recipe of $CsPbBr_3$ films, $CsPbCl_3$, $CsPbIBr_2$, and $CsPbI_2Br$ films were prepared by spin coating of 90 μL of $CsCl/H_2O$, CsI/H_2O, and $CsBr/H_2O$ onto $PbCl_2$, $PbBr_2$, and PbI_2 films, respectively. Photographs of the resulting films are given in the upper panel of Figure 5A. For comparison, photographs of the $CsPbCl_3$, $CsPbIBr_2$, and $CsPbI_2Br$ films prepared by the conventional two-step spin coating method are also provided in the bottom panel of Figure 5A. The color of the each of the films well consists with their bandgaps (Zhu et al., 2021; Zhu et al., 2020; Zhou et al., 2018). As expected, highly uniform $CsPbCl_3$, $CsPbIBr_2$, and $CsPbI_2Br$ films were obtained by the water-based spray-assisted growth strategy. The XRD patterns shown in Figure 5B reveal clear XRD peaks of (100), (110), and (200) planes in $CsPbCl_3$, $CsPbIBr_2$, and $CsPbI_2Br$ films, respectively, with no impurity phases. The UV-vis absorption spectra shown in Figure 5C indicate that $CsPbCl_3$, $CsPbIBr_2$, and $CsPbI_2Br$ films have absorption onsets of ~420, 613, and 645 nm, which correspond to bandgap values of ~2.95, 2.02, and 1.92 eV, respectively.

We also used the $CsPbCl_3$, $CsPbIBr_2$, and $CsPbI_2Br$ films to fabricate carbon-electrode, all-inorganic PSCs. The statistical PCEs of 20 independent PSCs based on $CsPbCl_3$, $CsPbIBr_2$, and $CsPbI_2Br$ films are shown in

Figure S3, wherein the average PCEs are (0.62 ± 0.22)%, (9.95 ± 0.23)%, and (12.54 ± 0.22)%, respectively. J-V curves of the best-performing PSCs based on $CsPbCl_3$, $CsPbIBr_2$, and $CsPbI_2Br$ films are shown in Figure 5D, and detailed photovoltaic parameters are given in Table S2. PCEs of 1.27%, 10.44%, and 13.30% were realized for PSCs fabricated with $CsPbCl_3$, $CsPbIBr_2$, and $CsPbI_2Br$ films, respectively, all of which rank among the highest-performing all-inorganic PSCs reported to date (Du et al., 2021; Zhu et al., 2021). In addition, the EQE spectra of the related PSCs in Figure S4 show that photocurrent onsets are well in accordance with the absorption characters of $CsPbCl_3$, $CsPbIBr_2$, and $CsPbI_2Br$ films, revealing that these inorganic perovskite films dominate their photoelectric conversion process. Overall, the aforementioned results make known that the proposed water-based spray-assisted growth strategy may be a universal approach to fabricating scalable, high-efficiency carbon-electrode, all-inorganic PSCs.

DISCUSSION

We developed a water-based spray-assisted growth method to prepare large-area all-inorganic perovskite films in this study. The proposed strategy is performed by directly spraying cesium halide water solution onto spin-coating-deposited lead halide films under ambient conditions, followed by thermal annealing. With $CsPbBr_3$ as an example, we show that the films feature uniform surface, full coverage, pure phase, large grains, and high crystallinity after adjusting the volume of $CsBr/H_2O$. These desired benefits of $CsPbBr_3$ films mainly originate from the controllable CsBr loading and the use of water as the CsBr solvent, which makes the reaction between CsBr and $PbBr_2$ immune to the underlying $PbBr_2$ film microstructure. Small-area carbon-electrode $CsPbBr_3$ PSCs with active area of 0.09 cm^2 yielded a PCE of 10.22% coupled with excellent operational stability in ambient air. We also achieved a PCE of 8.21% for the champion one with the aperture area of 1.00 cm^2. The PCEs we created for both small- and large-area $CsPbBr_3$ PSCs stand the highest values among previously reported PSCs with a similar configuration, which are assumed to be further improved by element doping or interface modification strategies. We also demonstrated that the proposed water-based spray-assisted deposition strategy is applicable for desired $CsPbCl_3$, $CsPbIBr_2$, and $CsPbI_2Br$ films, with superior PCEs of 1.27%, 10.44%, and 13.30%, respectively, for carbon-electrode PSCs. We thus provide generic guidance for scalable, high-efficiency carbon-electrode, all-inorganic PSCs as well as further advancements in all-inorganic perovskite optoelectronics.

Limitations of the study

Here, a generic water-based spray-assisted deposition strategy to produce all-inorganic perovskite films is demonstrated to enable scalable, high-efficiency carbon-electrode, all-inorganic PSCs. However, owing to the toxicity of PbX_2 (X= Cl, Br, or I) as well as its solvents, such as DMSO or DMF, PbX_2 films can only be produced by spin coating in a glove box instead of using spray-assisted strategy in ambient air. Therefore, we can currently prepare a large-area $CsPbBr_3$ film with a size of 10 × 10 cm^2, and the preparation conditions of the $PbBr_2$ film limit the further scaling up of its size. Besides, the highest PCE of the large-area $CsPbBr_3$ PSC prepared by proposed strategy was 8.21% lower than that of the small-area device, which was 10.22%. The deposition process for the larger area all-inorganic perovskite films and the performance optimization of PSCs based on them will be the direction of our continued research.

STAR★METHODS

Detailed methods are provided in the online version of this paper and include the following:

- KEY RESOURCES TABLE
- RESOURCE AVAILABILITY
  - Lead contact
  - Materials availability
  - Data and code availability
- METHODS DETAILS
  - Preparation of all-inorganic perovskite films
  - Fabrication of carbon-electrode PSCs
  - Characterizations
- QUANTIFICATION AND STATISTICAL ANALYSIS

SUPPLEMENTAL INFORMATION

Supplemental information can be found online at https://doi.org/10.1016/j.isci.2021.103365.

ACKNOWLEDGMENTS

The authors gratefully acknowledge the financial support from the National Natural Science Foundation of China (61804113, 61874083, and 62004151), the Initiative Postdocs Supporting Program (BX20190261), the China Postdoctoral Science Foundation (2019M663628), the National Natural Science Foundation of Shaanxi Province (2018ZDCXL-GY-08-02-02 and 2017JM6049), and the Joint Research Funds of Department of Science & Technology of Shaanxi Province and Northwestern Polytechnical University (No. 2020GXLH-Z-014).

AUTHOR CONTRIBUTIONS

W.Z. and C.Z. proposed and designed the experiments, J.Z. and Y.H. supervised the study, Z.Z. and Y.B. conducted the experiments, D.C. and J.M. performed the data collection, H.X. and D.C. fulfilled the analysis of experimental results, W.Z. and Z.Z. wrote the manuscript, and C.Z. and J.Z. helped to revise the manuscript. All authors discussed the results and commented on the manuscript.

DECLARATION OF INTERESTS

The authors declare no competing interests.

Received: August 12, 2021
Revised: September 15, 2021
Accepted: October 23, 2021
Published: November 19, 2021

REFERENCES

Bing, J., Huang, S., and Ho-Baillie, A.W.Y. (2020). A review on halide perovskite film formation by sequential solution processing for solar cell applications. Energy Technol. *8*, 1901114.

Chang, X., Li, W., Zhu, L., Liu, H., Geng, H., Xiang, S., Liu, J., and Chen, H. (2016). Carbon-based $CsPbBr_3$ perovskite solar cells: all-ambient processes and high thermal stability. ACS Appl. Mater. Interfaces *8*, 33649–33655.

Chen, W., Li, X., Li, Y., and Li, Y. (2020). A review: crystal growth for high-performance all-inorganic perovskite solar cells. Energy Environ. Sci. *13*, 1971–1996.

Cheng, Y., and Ding, L. (2021). Pushing commercialization of perovskite solar cells by improving their intrinsic stability. Energy Environ. Sci. *14*, 3233–3255.

Chi, W., and Banerjee, S.K. (2021). Stability improvement of perovskite solar cells by compositional and interfacial engineering. Chem. Mater. *33*, 1540–1570.

Dong, C., Han, X., Li, W., Qiu, Q., and Wang, J. (2019). Anti-solvent assisted multi-step deposition for efficient and stable carbon-based $CsPbI_2Br$ all-inorganic perovskite solar cell. Nano Energy *59*, 553–559.

Du, J., Duan, J., Yang, X., Duan, Y., Zhou, Q., and Tang, Q. (2021). P-Type charge transfer doping of graphene oxide with $(NiCo)_{1-y}Fe_yO_x$ for air-stable, all-inorganic $CsPbIBr_2$perovskite solar cells. Angew. Chem. *133*, 10702–10707.

Duan, J., Zhao, Y., He, B., and Tang, Q. (2018a). High-purity inorganic perovskite films for solar cells with 9.72% efficiency. Angew.Chem. *130*, 3849–3853.

Duan, J., Dou, D., Zhao, Y., Wang, Y., Yang, X., Yuan, H., He, B., and Tang, Q. (2018b). Spray-assisted deposition of $CsPbBr_3$ films in ambient air for large-area inorganic perovskite solar cells. Mater.Today Energy *10*, 146–152.

Duan, J., Wang, Y., Yang, X., and Tang, Q. (2020). Alkyl-chain-regulated charge transfer in fluorescent inorganic $CsPbBr_3$perovskite solar cells. Angew.Chem. Int. Ed. *59*, 4391–4395.

Faheem, M.B., Khan, B., Feng, C., Farooq, M.U., Raziq, F., Xiao, Y., and Li, Y. (2019). All-inorganic perovskite solar cells: energetics, key challenges, and strategies toward commercialization. ACS Energy Lett *5*, 290–320.

Feng, J., Han, X., Huang, H., Meng, Q., Zhu, Z., Yu, T., Li, Z., and Zou, Z. (2020). Curing the fundamental issue of impurity phases in two-step solution-processed $CsPbBr_3$ perovskite films. Sci. Bull. *65*, 726–737.

Guo, H., Pei, Y., Zhang, J., Cai, C., Zhou, K., and Zhu, Y. (2019). Doping with $SnBr_2$ in $CsPbBr_3$ to enhance the efficiency of all-inorganic perovskite solar cells. J. Mater. Chem. C *7*, 11234–11243.

He, J., Liu, J., Hou, Y., Wang, Y., Yang, S., and Yang, H.G. (2020). Surface chelation of cesium halide perovskite by dithiocarbamate for efficient and stable solar cells. Nat. Commun. *11*, 1–8.

Heo, J.H., Zhang, F., Xiao, C., Heo, S.J., Park, J.K., Berry, J.J., Zhu, K., and Im, S.H. (2021). Efficient and stable graded $CsPbI_{3-x}Br_x$perovskite solar cells andsubmodules by orthogonal processable spray coating. Joule *5*, 481–494.

Ho-Baillie, A., Zhang, M., Lau, C.F.J., Ma, F.-J., and Huang, S. (2019). Untapped potentials of inorganic metal halide perovskite solar cells. Joule *3*, 938–955.

Hu, Y., Chu, Y., Wang, Q., Zhang, Z., Ming, Y., Mei, A., Rong, Y., and Han, H. (2019). Standardizing perovskite solar modules beyond cells. Joule *3*, 2076–2085.

Kojima, A., Teshima, K., Shirai, Y., and Miyasaka, T. (2009). Organometal halide perovskites as visible-light sensitizers for photovoltaic cells. J. Am. Chem. Soc. *131*, 6050–6051.

Krebs, F.C. (2009). Fabrication and processing of polymer solar cells: a review of printing and coating techniques. Sol. Energy Mater. Solar Cells *93*, 394–412.

Lau, C.F.J., Deng, X., Ma, Q., Zheng, J., Yun, J.S., Green, M.A., Huang, S., and Ho-Baillie, A.W.Y. (2016). $CsPbIBr_2$perovskite solar cell by spray-assisted deposition. ACS Energy Lett. *1*, 573–577.

Lee, S.W., Bae, S., Kim, D., and Lee, H.S. (2020). Historical analysis of high-efficiency, large-area solar cells: toward upscaling of perovskite solar cells. Adv. Mater. *32*, 2002202.

Li, Z., Klein, T.R., Kim, D.H., Yang, M., Berry, J.J., van Hest, M.F.A.M., and Zhu, K. (2018). Scalable fabrication of perovskite solar cells. Nat. Rev. Mater. *3*, 18017.

Li, X., Tan, Y., Lai, H., Li, S., Chen, Y., Li, S., Xu, P., and Yang, J. (2019). All-inorganic $CsPbBr_3$ perovskite solar cells with 10.45% efficiency by evaporation-assisted deposition and setting intermediate energy levels. ACS Appl. Mater. Interfaces *11*, 29746–29752.

Li, N., Niu, X., Chen, Q., and Zhou, H. (2020). Towards commercialization: the operational stability of perovskite solar cells. Chem. Soc. Rev. *49*, 8235–8286.

Li, D., Zhang, D., Lim, K.S., Hu, Y., Rong, Y., Mei, A., Park, N.G., and Han, H. (2021). A review on

scaling up perovskite solar cells. Adv. Funct. Mater. *31*, 2008621.

Liang, J., Wang, C., Wang, Y., Xu, Z., Lu, Z., Ma, Y., Zhu, H., Hu, Y., Xiao, C., and Yi, X. (2016). All-inorganic perovskite solar cells. J. Am. Chem. Soc. *138*, 15829–15832.

Lin, Z.Q., Qiao, H.W., Zhou, Z.R., Hou, Y., Li, X., Yang, H.G., and Yang, S. (2020). Water assisted formation of highly oriented $CsPbI_2Br$ perovskite films with the solar cell efficiency exceeding 16%. J. Mater. Chem. A. *8*, 17670–17674.

Liu, X., Tan, X., Liu, Z., Ye, H., Sun, B., Shi, T., Tang, Z., and Liao, G. (2019a). Boosting the efficiency of carbon-based planar $CsPbBr_3$ perovskite solar cells by a modified multistep spin-coating technique and interface engineering. Nano Energy *56*, 184–195.

Liu, J., Zhu, L., Xiang, S., Wei, Y., Xie, M., Liu, H., Li, W., and Chen, H. (2019b). Growing high-quality $CsPbBr_3$ by using porous $CsPb_2Br_5$ as an intermediate: a promising light absorber in carbon-based perovskite solar cells. Sustain. Energy Fuels *3*, 184–194.

Liu, F.-W., Biesold, G., Zhang, M., Lawless, R., Correa-Baena, J.-P., Chueh, Y.-L., and Lin, Z. (2021). Recycling and recovery of perovskite solar cells. Mater. Today *43*, 185–197.

Luo, P., Zhou, Y., Zhou, S., Lu, Y., Xu, C., Xia, W., and Sun, L. (2018). Fast anion-exchange from $CsPbI_3$ to $CsPbBr_3$ via Br_2-vapor-assisted deposition for air-stable all-inorganic perovskite solar cells. Chem. Eng. J. *343*, 146–154.

Luo, D., Su, R., Zhang, W., Gong, Q., and Zhu, R. (2020). Minimizing non-radiative recombination losses in perovskite solar cells. Nat. Rev. Mater. *5*, 44–60.

Park, N.-G., and Zhu, K. (2020). Scalable fabrication and coating methods for perovskite solar cells and solar modules. Nat. Rev. Mater. *5*, 333–350.

Qiu, L., He, S., Ono, L.K., Liu, S., and Qi, Y. (2019). Scalable fabrication of metal halide perovskite solar cells and modules. ACS Energy Lett. *4*, 2147–2167.

Remeika, M., and Qi, Y. (2018). Scalable solution coating of the absorber for perovskite solar cells. J. Energy Chem. *27*, 1101–1110.

Rong, Y., Hu, Y., Mei, A., Tan, H., Saidaminov, M.I., Seok, S.I., McGehee, M.D., Sargent, E.H., and Han, H. (2018). Challenges for commercializing perovskite solar cells. Science *361*, eaat8235.

Sutton, R.J., Eperon, G.E., Miranda, L., Parrott, E.S., Kamino, B.A., Patel, J.B., Hörantner, M.T., Johnston, M.B., Haghighirad, A.A., and Moore, D.T. (2016). Bandgap-tunable cesium lead halide perovskites with high thermal stability for efficient solar cells. Adv. Energy Mater. *6*, 1502458.

Swartwout, R., Hoerantner, M.T., and Bulović, V. (2019). Scalable deposition methods for large-area production of perovskite thin films. Energy Environ. Mater. *2*, 119–145.

Teng, P., Han, X., Li, J., Xu, Y., Kang, L., Wang, Y., Yang, Y., and Yu, T. (2018). Elegant face-down liquid-space-restricted deposition of $CsPbBr_3$ films for efficient carbon-based all-inorganic planar perovskite solar cells. ACS Appl. Mater. Interfaces *10*, 9541–9546.

Tian, J., Xue, Q., Yao, Q., Li, N., Brabec, C.J., and Yip, H.L. (2020). Inorganic halide perovskite solar cells: progress and challenges. Adv. Energy Mater. *10*, 2000183.

Tong, G., Chen, T., Li, H., Qiu, L., Liu, Z., Dang, Y., Song, W., Ono, L.K., Jiang, Y., and Qi, Y. (2019a). Phase transition induced recrystallization and low surface potential barrier leading to 10.91%-efficient $CsPbBr_3$ perovskite solar cells. Nano Energy *65*, 104015.

Tong, G., Chen, T., Li, H., Song, W., Chang, Y., Liu, J., Yu, L., Xu, J., Qi, Y., and Jiang, Y. (2019b). High efficient hole extraction and stable all-bromide inorganic perovskite solar cells via derivative-phase gradient bandgap architecture. Sol. RRL *3*, 1900030.

Wang, H., Liu, H., Dong, Z., Li, W., Zhu, L., and Chen, H. (2021). Composition manipulation boosts the efficiency of carbon-based $CsPbI_3$ perovskite solar cells to beyond 14%. Nano Energy *84*, 105881.

Xiang, S., Fu, Z., Li, W., Wei, Y., Liu, J., Liu, H., Zhu, L., Zhang, R., and Chen, H. (2018). Highly air-stable carbon-based α-$CsPbI_3$ perovskite solar cells with a broadened optical spectrum. ACS Energy Lett. *3*, 1824–1831.

Xiang, S., Li, W., Wei, Y., Liu, J., Liu, H., Zhu, L., Yang, S., and Chen, H. (2019). Natrium doping pushes the efficiency of carbon-based $CsPbI_3$ perovskite solar cells to 10.7%. Iscience *15*, 156–164.

Yu, Y.-T., Yang, S.-H., Chou, L.-H., Osaka, I., Wang, X.-F., and Liu, C.-L. (2021). One-step spray-coated all-inorganic $CsPbI_2Br$ perovskite solar cells. ACS Appl. Energy Mater. *1*, 573–577.

Zhang, L., and Lin, S. (2020). Dimensional tailoring of halide perovskite: a case study on Cs_4PbBr_6/$CsPbBr_3$ hybrid with molecular halide perovskite. Sol. Energy Mater.Sol. Cells *204*, 110237.

Zhang, T., Yang, M., Zhao, Y., and Zhu, K. (2015). Controllable sequential deposition of planar $CH_3NH_3PbI_3$ perovskite films via adjustable volume expansion. Nano Lett. *15*, 3959–3963.

Zhang, X., Jin, Z., Zhang, J., Bai, D., Bian, H., Wang, K., Sun, J., Wang, Q., and Liu, S.F. (2018). All-ambient processed binary $CsPbBr_3$–$CsPb_2Br_5$ perovskites with synergistic enhancement for high-efficiency Cs–Pb–Br-based solar cells. ACS Appl. Mater. Interfaces *10*, 7145–7154.

Zhang, Y., Luo, L., Hua, J., Wang, C., Huang, F., Zhong, J., Peng, Y., Ku, Z., and Cheng, Y.-b. (2019). Moisture assisted $CsPbBr_3$ film growth for high-efficiency, all-inorganic solar cells prepared by a multiple sequential vacuum deposition method. Mater. Sci. Semicond.Process. *98*, 39–43.

Zhang, G., Xie, P., Huang, Z., Yang, Z., Pan, Z., Fang, Y., Rao, H., and Zhong, X. (2021). Modification of energy level alignment for boosting carbon-based $CsPbI_2Br$ solar cells with 14% certified efficiency. Adv. Funct. Mater. *31*, 2011187.

Zhou, H., Fan, L., He, G., Yuan, C., Wang, Y., Shi, S., Sui, N., Chen, B., Zhang, Y., and Yao, Q. (2018). Low defects, large area and high stability of all-inorganic lead halide perovskite $CsPbBr_3$ thin films with micron-grains via heat-spraying process for self-driven photodetector. RSC Adv. *8*, 29089–29095.

Zhu, W., Zhang, Q., Chen, D., Zhang, Z., Lin, Z., Chang, J., Zhang, J., Zhang, C., and Hao, Y. (2018). Intermolecular exchange boosts efficiency of air-stable, carbon-based all-inorganic planar $CsPbIBr_2$perovskite solar cells to over 9%. Adv. Energy Mater. *8*, 1802080.

Zhu, W., Deng, M., Chen, D., Zhang, Z., Chai, W., Chen, D., Xi, H., Zhang, J., Zhang, C., and Hao, Y. (2020). Dual-phase $CsPbCl_3$–Cs_4PbCl_6 perovskite films for self-powered, visible-blind UV photodetectors with fast response. ACS Appl. Mater. Interfaces *12*, 32961–32969.

Zhu, W., Chai, W., Chen, D., Ma, J., Chen, D., Xi, H., Zhang, J., Zhang, C., and Hao, Y. (2021). High-efficiency (> 14%) and air-stable carbon-based, all-inorganic $CsPbI_2Br$ perovskite solar cells through a top-seeded growth strategy. ACS Energy Lett. *6*, 1500–1510.

STAR★METHODS

KEY RESOURCES TABLE

REAGENT or RESOURCE	SOURCE	IDENTIFIER
$PbBr_2$	Alfa-Aesar	CAS: 10031-22-8
PbI_2	Alfa-Aesar	CAS: 10101-63-0
CsBr	Alfa-Aesar	CAS: 7787-69-1
$PbCl_2$	Xi'an Polymer Light Co., Ltd.	CAS: 7758-95-4
CsCl	Xi'an Polymer Light Co., Ltd.	CAS: 7647-17-8
DMF	Sigma-Aldrich	CAS: 68-12-2
Conductive carbon paste	Shanghai MaterWin New Materials Co., Ltd.	http://www.materwin.com/
FTO glass	Pilkington TEC Glass	https://www.p-oled.cn/index/zh-hans/

RESOURCE AVAILABILITY

Lead contact

Further information and requests for resources should be directed to and will be fulfilled by the lead contact, Dr. Weidong Zhu (wdzhu@xidian.edu.cn).

Materials availability

This study did not generate new materials.

Data and code availability

All data reported in this paper will be shared by the lead contact upon request.

This paper does not report original code.

Any additional information required to reanalyze the data reported in this paper is available from the lead contact upon request.

METHODS DETAILS

Preparation of all-inorganic perovskite films

FTO substrate (2 × 2.5 cm^2) was sequentially cleaned in detergent, deionized water, acetone, and ethanol with sonication, and finally were dried under N_2 stream. After further 15 min of ultraviolet ozone treatment, a ~60 nm of TiO_2 layer was deposited on FTO substrate by spin-coating of TiO_2 sol at 3000 rpm for 30 s and thermal annealing at 500°C for 1 h in air. Then, 100 μL of $PbCl_2$, $PbBr_2$, or PbI_2 solution was spin-coated onto TiO_2/FTO substrate at 2000 rpm for 30 s in a glovebox (pO_2, pH_2O < 1 ppm), wherein the $PbCl_2$, $PbBr_2$, or PbI_2 solution was prepared by dissolving of 278 mg $PbCl_2$, 367 mg $PbBr_2$, and 461mg PbI_2 into 1mL DMF at 90°C with vigorous stir. After the thermal treatment at 90°C for 30 min, the $PbCl_2$, $PbBr_2$, or PbI_2 film was obtained. Next, 90 μL of cesium halide water solution was sprayed onto lead halide film in ambient air by using a commercial airbrush, which was connected to N_2 gas with the pressure of 15 psi. To be specific, the 168 mg/mL CsCl/H_2O and $PbCl_2$ film were adopted to obtain the $CsPbCl_3$ film; the 250 mg/mL CsBr/H_2O and $PbBr_2$ were used to prepare the $CsPbBr_3$ film; the 260 mg/mL CsI/H_2O and $PbBr_2$ were employed to produce the $CsPbIBr_2$ film; the 250 mg/mL CsBr/H_2O and PbI_2 were utilized to form the $CsPbI_2Br$ film. After the spray coating procedure, all the samples were annealed at 250°C for 5 min in ambient air to promote the reaction between cesium halide and lead halide.

Fabrication of carbon-electrode PSCs

Finally, the commercial conductive carbon paste was screen-printed onto the $CsPbCl_3$, $CsPbBr_3$, $CsPbIBr_2$, or $CsPbI_2Br$ film in ambient air. The area of carbon paste pattern was fixed to be 0.09 or 1.00 cm^2. With the thermal treatment at 120°C for 15 min in ambient air, the carbon electrode can be formed, and hence a carbon-electrode, all-inorganic PCS can be achieved successfully.

Characterizations

SEM images were obtained by a Zeiss Supra-40 field-emission SEM instrument (Carl Zeiss SMT AG, Germany). XRD patterns were collected from the samples by a D8-advance X-ray diffractometer (Bruker, Germany). A PerkinElmer spectrophotometer was used to record the UV-visible absorption spectra. Steady-state PL spectra were obtained by a Delta Flex fluorescence lifetime system (Horiba Scientific Com., Japan) with an excitation at 478 nm. J-V characteristics were measured by a Keithley 2450 source-meter, during which the PSCs were placed under a simulated AM 1.5G irradiation generated by an Oriel 92251A-1000 solar simulator in ambient air. EQE data were acquired in ambient air by using a solar-cell spectral-response measurement system (Cornerstone 74004) equipped with a 150 W xenon lamp (Oriel).

QUANTIFICATION AND STATISTICAL ANALYSIS

To compare the device performance changes, the photovoltaic parameters reported in this work are the average values of multiple PSCs under the same conditions.